*Article*

# Preparation and Characterization of ZnO Nanoparticles Supported on Amorphous SiO$_2$

**Ying Chen, Hao Ding * and Sijia Sun**

Beijing Key Laboratory of Materials Utilization of Nonmetallic Minerals and Solid Wastes, National Laboratory of Mineral Materials, School of Materials Science and Technology, China University of Geosciences (Beijing), Beijing 100083, China; chenying@cugb.edu.cn (Y.C.); 1012122105@cugb.edu.cn (S.S.)
* Correspondence: dinghao113@126.com; Tel.: +86-010-8232-2982

**Abstract:** In order to reduce the primary particle size of zinc oxide (ZnO) and eliminate the agglomeration phenomenon to form a monodisperse state, $Zn^{2+}$ was loaded on the surface of amorphous silica (SiO$_2$) by the hydrogen bond association between hydroxyl groups in the hydrothermal process. After calcining the precursors, dehydration condensation among hydroxyl groups occurred and ZnO nanoparticles supported on amorphous SiO$_2$ (ZnO–SiO$_2$) were prepared. Furthermore, the SEM and TEM observations showed that ZnO nanoparticles with a particle size of 3–8 nm were uniformly and dispersedly loaded on the surface of amorphous SiO$_2$. Compared with pure ZnO, ZnO–SiO$_2$ showed a much better antibacterial performance in the minimum inhibitory concentration (MIC) test and the antibacterial properties of the paint adding ZnO–SiO$_2$ composite.

**Keywords:** amorphous SiO$_2$; load; monodisperse; ZnO nanoparticle; antibacterial

## 1. Introduction

Antimicrobial tests and environmental toxicity tests have been widely explored in order to improve health, safety, and the environment [1–3]. Zinc oxide (ZnO), as a semiconductor material with a band gap of 3.3 eV at room temperature [4], has high chemical stability, strong photosensitivity and non-toxicity property and is widely used in antibacterial materials [5]. Compared with ordinary ZnO powder, ZnO nanoparticles have a large specific surface area and small size effect, and show wide application potential in microbial inhibition and mildew removal [6,7].

However, like most of the nanoparticles, ZnO nanoparticles are prone to forming serious agglomeration, including hard agglomeration among the particles formed via the chemical reaction of the surface groups and soft agglomeration formed by other physical effects [8]. It is difficult to depolymerize the particles involved in hard agglomeration. Therefore, the apparent grain size of the primary ZnO particles tends to increase to the micron scale and the normal performance of ZnO nanoparticles is inhibited. In the preparation process of ZnO nanoparticles, in addition to the control of the ZnO morphology and primary particle size, the agglomeration phenomenon of ZnO particles should be suppressed to obtain dispersed nanoparticles. Wang et al. synthesized the doped ZnO nanoparticles with the mixture of alcohol and water as the solvent according to a precipitation method [9]. Chen et al. prepared ZnO nanocrystals via the reaction of zinc stearate with excessive alcohol in the hydrocarbon solvent [10]. Weller et al. used the low-temperature solvent thermal method to synthesize dispersible spherical ZnO nanoparticles and nano-rods with zinc acetate as precursors in methanol [11]. However, these methods have low synthesis performance and limited control ability. Especially, the solvent thermal process [12,13] is required to deal with organic solvents and it is difficult to realize industrial production. Therefore, some nanoparticles (such as titanium dioxide, TiO$_2$) [14,15] are supported on the surface or pores of the inorganic carrier. In this way, the strong interaction between the carrier surface and nanoparticles, and the forced isolation among the carrier particles

efficiently prevent the agglomeration among the nanoparticles and improve the dispersion effects and functions.

Amorphous $SiO_2$, commercially known as white carbon black, is an aggregate of $SiO_2$ particles ($SiO_2 \cdot nH_2O$) and commonly used as a rubber reinforcing additive [16,17]. The primary particle size of $SiO_2$ particles is generally 10–100 nm. $SiO_2$ particles containing rich Si–OH groups, which can form a strong interaction between the $SiO_2$ carrier surface and Zn–OH (precursors of ZnO). This interaction reduces the combination between Zn–OH and prevents its aggregation, thus contributing to the formation of monodisperse ZnO nanoparticles. In addition, small amorphous $SiO_2$ particles have high dispensability and can prevent further agglomeration of ZnO–$SiO_2$ composite. Therefore, amorphous $SiO_2$ was selected as the carrier of supported ZnO nanoparticles.

Based on the above results, in this paper, the environmentally friendly hydrothermal method was adopted to prepare ZnO–$SiO_2$ by loading $Zn^{2+}$ on the surface of amorphous $SiO_2$ and calcining active products at high temperatures. Moreover, the structures and antibacterial properties of as-prepared ZnO–$SiO_2$ were explored.

## 2. Experimental Procedure

### 2.1. Materials

In this study, amorphous $SiO_2$ was purchased from Henan Jiaozuo Fluoride New Energy Technology Co., Ltd (Jiaozuo, Henan, China). The properties of amorphous $SiO_2$ are described as follows: $SiO_2$ content of 96.63%, whiteness of 96.76%, average aggregate size of 20 µm, primary particle size of 20–30 nm, and specific surface area of 59.54 $m^2/g$. Zinc nitrate ($Zn(NO_3)_2 \cdot 6H_2O$) as the source of $Zn^{2+}$ was from Beijing Yili Fine Chemical Co., Ltd (Beijing, China). Sodium polyacrylate (PAAS) as a dispersant was supplied by Changzhou Run Yang Chemical Co., Ltd (Changzhou, Jiangsu, China). Pure ZnO, as an antibacterial agent, was compared with the ZnO–$SiO_2$ composite in antibacterial performance. It was produced by the Xi Long Chemical Co., Ltd (Guangzhou, Guangdong, China) and the size of the particles was about 200 nm. Figure 1 shows SEM images of amorphous $SiO_2$ and pure ZnO.
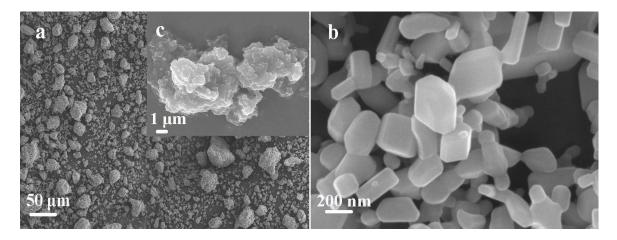


**Figure 1.** Micrographs of (**a**,**c**) amorphous $SiO_2$ and (**b**) pure ZnO.

### 2.2. ZnO–$SiO_2$ Precursor

Amorphous $SiO_2$, sodium polyacrylate (1% of the weight of $SiO_2$) and $H_2O$ were mixed and stirred to prepare the suspension with solid content of 18%. Ceramic polishing balls (diameter: 1–3 mm) were added into the suspension according to the proportion of 50% of the solid content and then stirred at a speed of 1000 r/min for 1 h to prepare the depolymerized amorphous $SiO_2$ slurry. A zinc nitrate solution (0.09 wt %) was added into the slurry and the pH of the mixture was respectively

adjusted to 5.0 and 7.0 by adding 6 mol/L NaOH and 6 mol/L HNO$_3$. The mixture was stirred at 60 °C for 1 h. The precursors were obtained after suction filtration, washing, and drying and denoted as Zn–SiO$_2$-pH5.0 (the precursor was prepared with pH value at 5.0) and Zn–SiO$_2$-pH7.0 (the precursor was prepared with pH value at 7.0) respectively. The preparation process is shown in Figure 2.

### 2.3. Preparation of ZnO–SiO$_2$

The precursors Zn–SiO$_2$-pH5.0 and Zn-SiO$_2$-pH7.0 were calcined at 400 °C for 1 h to obtain the composite particles of ZnO and SiO$_2$ and denoted as ZnO–SiO$_2$-pH5.0 (the composite obtained by calcining the precursor which was prepared with pH value at 5.0) and ZnO–SiO$_2$-pH7.0 (the composite obtained by calcining the precursor which was prepared with pH value at 7.0). The loads of ZnO were 4.51 and 11.26%, respectively.
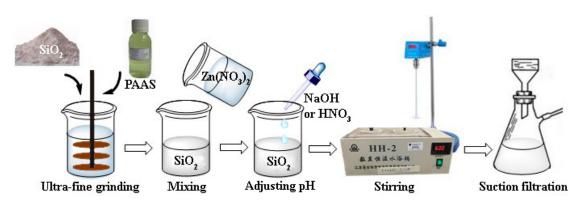


**Figure 2.** Preparation of composite particles of ZnO–SiO$_2$ precursor.

### 2.4. Characterization

The X-ray diffraction (XRD) was measured by using a D/max-Ra X-ray diffractometer (Ouyatu, Japan, Cu K$\alpha$ radiation = 1.54 Å) in an angular range of 10–80° (2θ) with a step of 0.02° (2θ). Scherer Equation [18] is used to calculate the average grain size of ZnO nanoparticles:

$$\beta = \frac{K\lambda}{Dcos\theta''} \tag{1}$$

where *K* is the shape factor constant (0.94); $\lambda$ is X-ray wavelength; *D* is the grain size; $\theta$ is the diffraction angle; $\beta$ is the diffraction peak half width.

An X-ray fluorescence spectrometer (XRF Shimadzu-1800, Kyoto, Japan) was used to analyze the oxide content of samples. The particle size and size distribution of the composite particles of ZnO and SiO$_2$ were characterized by transmission electron microscopy (TEM FEI Tecnai G220, Portland, OR, USA). Scanning electron microscopy (SEM) was used to explore the morphology of ZnO–SiO$_2$ by a Hitachi field emission scanning electron microscope (Hitachi S4800, Tokyo, Japan) under the voltage of 10 kV. The Fourier transform infrared spectroscopy (FTIR, Madison, WI, USA) measurement was carried out to explore the changes in functional groups of ZnO-SiO$_2$ by Nicolet IS50. The samples were finely pulverized and then diluted in dried KBr to form a homogeneous mixture according to the sample-KBr ratio of 1/200. The X-ray photoelectron spectroscopy (XPS, Manchester, UK) measurement was conducted on an Axis Ultra spectrometer with monochromatic Mg K$\alpha$ (1253.6 eV) radiation to investigate the valence state of Zn.

### 2.5. Antimicrobial Test

The antimicrobial ability of ZnO–SiO$_2$ under dark conditions was investigated through antibacterial tests [19–21]. Different concentrations of ZnO–SiO$_2$-pH5.0, ZnO–SiO$_2$-pH7.0, and pure

ZnO were added to the agar medium, and then *E. coli* (CGMCC 1.2385) was inoculated on the medium to observe the growth of bacteria and determine the minimum inhibitory concentration (MIC) [22].

The antimicrobial coating was obtained by mixing 12 wt % styrene-acrylic emulsion, 34 wt % of $H_2O$, 50 wt % of the filler (0–8 wt % of ZnO–$SiO_2$-pH7.0), and 4 wt % of paint additive. The antibacterial property of ZnO–$SiO_2$ was evaluated by testing the antibacterial property of the coating. The antibacterial rate of the coating was tested according to Chinese national standard GB/T21866-2008 [23]. The antibacterial rate (R) is calculated as:

$$R = 100\% \times (A - B)/A, \tag{2}$$

where *A* and *B* are the average number of colonies of the blank control plate and antibacterial coating plate after 24 h.

## 3. Results and Discussion

### *3.1. Structure and Characterization of ZnO–$SiO_2$*

#### 3.1.1. Phase and Chemical Constitution of ZnO–$SiO_2$

Figure 3 shows the XRD patterns of ZnO–$SiO_2$. Table 1 shows the XRF results of each sample. The XRD pattern of the $SiO_2$ carrier shows a strong bread peak near $2\theta$ of 23°, indicating that the main phase is an amorphous phase corresponding to amorphous $SiO_2$. In the XRD patterns of ZnO–$SiO_2$-pH5.0 and ZnO–$SiO_2$-pH7.0, in addition to the above-mentioned peak reflecting the amorphous phase, the peaks at 31.8°, 34.5°, 36.3°, and 47.5° correspond to the ZnO diffraction peak [24,25], indicating that $Zn^{2+}$ has been transformed into ZnO after the thermal reaction with the $SiO_2$ carrier and calcination. The ZnO diffraction intensity of ZnO–$SiO_2$-pH7.0 was significantly larger than that of ZnO–$SiO_2$-pH5.0 due to the different loadings of ZnO. The contents of ZnO in ZnO–$SiO_2$-pH5.0 and ZnO–$SiO_2$-pH7.0 are respectively 4.51 and 11.26% (Table 1). The $SiO_2$ content in ZnO–$SiO_2$-pH5.0 is lower than that in ZnO–$SiO_2$-pH7.0. The results are consistent with the XRD results.
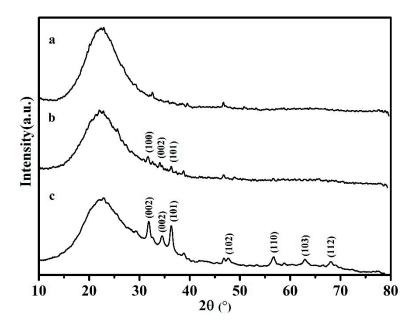


**Figure 3.** XRD of (**a**) amorphous $SiO_2$; (**b**) ZnO–$SiO_2$-pH5.0; and (**c**) ZnO–$SiO_2$-pH7.0.

**Table 1.** XRF of amorphous $SiO_2$, $ZnO–SiO_2$-pH5.0 and $ZnO–SiO_2$-pH7.0.

| Samples | $SiO_2$/% | ZnO/% | $Na_2O$/% |
|---|---|---|---|
| amorphous $SiO_2$ | 96.63 | 0 | 0.98 |
| $ZnO–SiO_2$-pH5.0 | 92.78 | 4.51 | 1.05 |
| $ZnO–SiO_2$-pH7.0 | 84.22 | 11.26 | 2.68 |

According to the XRD data in Figure 3, the grain size of $ZnO–SiO_2$-pH7.0 was calculated to be 3.63 nm according to the Scherer Equation.

### 3.1.2. Microstructure of $ZnO–SiO_2$

Figure 4 shows the distribution of three elements (O, Si, and Zn) in $ZnO–SiO_2$-pH5.0 and $ZnO–SiO_2$-pH7.0. The distributions of these three elements are consistent with the distribution of $ZnO–SiO_2$ particles. The distribution densities of O and Si are larger than that of Zn. The Zn density in the elemental distribution of $ZnO–SiO_2$-pH7.0 is greater than that of $ZnO–SiO_2$-pH5.0. The results indicate that the main components of $ZnO–SiO_2$ are $SiO_2$. The content of ZnO is low, but evenly distributed on the surface of $SiO_2$ particles.

Figure 5 shows the TEM images of the amorphous $SiO_2$ carrier, $ZnO–SiO_2$-pH5.0, and $ZnO–SiO_2$-pH7.0. At a small scale, all the samples are regular particle aggregates. The particle size is about 20–30 nm. Although these particles overlap each other, the overall dispersion effect is good. These unit particles are obviously amorphous $SiO_2$ particles. At the scale of 10 nm, the surface morphology of $SiO_2$ particles in the $SiO_2$ carrier is uniform, indicating that no other material is loaded. At the scale of 2 nm, only homogeneous non-crystal phase particles are observed. Dark spots with a size of 3–8 nm are uniformly distributed in $ZnO–SiO_2$-PH5.0 and $ZnO–SiO_2$-pH7.0 at the scale of 10 nm. These dark spots are crystal phase particles at the larger magnification. The stripe spacing can reflect the lattice size. The stripe spacing of $ZnO–SiO_2$-pH5.0 and $ZnO–SiO_2$-pH7.0 are respectively measured to be 2.45 and 2.59 nm. ZnO (101) plane spacing and ZnO (002) plane spacing are respectively measured to be 2.45 and 2.59 Å, which are almost consistent with standard ZnO (101) plane spacing of 2.47 Å and ZnO (002) plane spacing of 2.60 Å (ICDD card # 89-7102). These data indicate that these ZnO nanoparticles were monodispersedly loaded on the $SiO_2$ surface. The size of ZnO particles is 3–8 nm, which is consistent with the average particle size of 3.63 nm obtained in the XRD test [18].
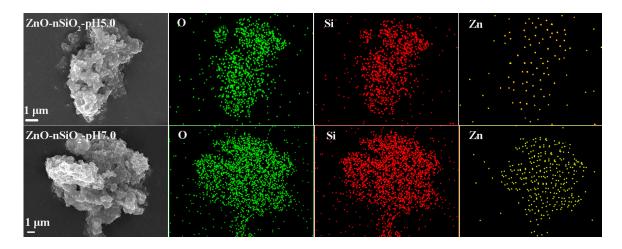


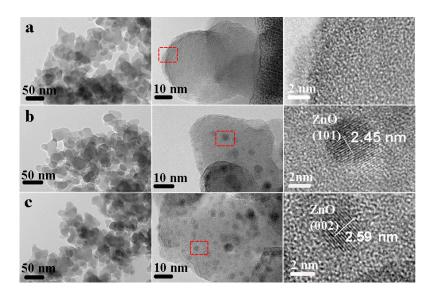**Figure 4.** SEM images of $ZnO–SiO_2$ and corresponding mapping results.

**Figure 5.** TEM maps of (**a**) amorphous $SiO_2$; (**b**) ZnO–$SiO_2$-pH5.0; (**c**) ZnO–$SiO_2$-pH7.0 at different scales.

### 3.1.3. Formation Mechanism of ZnO–$SiO_2$

Figure 6 shows the XPS pattern between 1015 and 1050 eV of the ZnO–$SiO_2$. The peaks of ZnO–$SiO_2$-pH5.0 and ZnO–$SiO_2$-pH7.0 at 1046.0 and 1045.5 eV correspond to $Zn2p_{1/2}$ orbital; the peaks at 1023.0 and 1022.5 eV correspond to the $Zn2p_{3/2}$ orbital [26]. These peaks are equivalent to the $2p_{1/2}$ and $2p_{3/2}$ energy peaks (1044.2 and 1021.2 eV) of ZnO [27]. Moreover, the energy difference between $Zn2p_{1/2}$ and $Zn2p_{3/2}$ orbitals is 23 eV, which is the same as that of ZnO. Therefore, it can be determined that the valence of Zn in ZnO–$SiO_2$-pH5.0 and ZnO–$SiO_2$-pH7.0 is +2, which is consistent with the results of XRD, XRF, and TEM.

Table 2 shows the percentages of the amorphous $SiO_2$ carrier, composite precursors (pH 5.0 and 7.0) and ZnO–$SiO_2$ based on XPS. Compared with the amorphous $SiO_2$ carrier, the $Zn^{2+}$ composite precursors show the increasing ratio of O/Si with the increase in the Zn content. The change may be interpreted as follows. Hydroxyl groups generated by the hydrolysis of Zn form hydrogen bonds on the $SiO_2$ surface, thus resulting in an increase in the amount of O. Compared with the precursors, ZnO–$SiO_2$ products show a decreased O/Si ratio because the amount of oxygen is decreased by the dehydration condensation reaction among the –OH bonds on the surface of precursors during calcination. The above analysis suggests that ZnO nanoparticles was loaded on the surface of amorphous $SiO_2$.

Figure 7 shows the infrared spectra of the amorphous $SiO_2$ carrier, $Zn^{2+}$ composite precursor (Zn–$SiO_2$-pH5.0 and Zn–$SiO_2$-pH7.0), and the final products (ZnO–$SiO_2$-pH5.0 and ZnO–$SiO_2$-pH7.0). The absorption peaks of each sample at 450 and 1062 $cm^{-1}$ are respectively ascribed to symmetrical and antisymmetric stretching vibration of Si–O–Si. The absorption peak at 799 $cm^{-1}$ corresponds to bending vibration, reflecting the characteristics of $SiO_2$ [28]. As shown in Figure 7, the infrared spectra of $Zn^{2+}$ composite precursors (Zn–$SiO_2$-pH5.0 and Zn–$SiO_2$-pH7.0) at 3317 and 3319 $cm^{-1}$ correspond to Zn–OH stretching vibration. The absorption peaks of hydroxyl groups in zinc hydroxide ($Zn(OH)_2$) at 1345 and 1347 $cm^{-1}$ reflect the bridging effect of the hydroxyl group in the product, and the Si–OH bending vibration peak in the two products moves from 958 $cm^{-1}$ (the vibration peak of the raw material $SiO_2$) to 952 and 954 $cm^{-1}$, respectively. The changes indicate that in the hydrothermal reaction during the preparation process of Zn–$SiO_2$-pH5.0, $Zn^{2+}$ forms a complex of $Zn(OH)_2$, which yields hydrogen bonds with Si–OH on the surface of amorphous $SiO_2$ [29–31]. In addition, the –OH bending vibration peaks of water adsorbed on the surface of Zn–$SiO_2$-pH5.0 and Zn–$SiO_2$-pH7.0 occur at 1413 and 1411 $cm^{-1}$, respectively. The –OH shear vibration peaks occur at 1580 and 1579 $cm^{-1}$ [32]. The Zn–OH and Si–OH of calcined products and the –OH bond of adsorbed water disappeared after the calcination of the precursors. Therefore, the high-temperature calcination resulted in the

evaporation of $SiO_2$ surface water and the dehydration condensation reaction between Si–OH and Zn–OH, and yielded Si–O–Zn chemical bond.
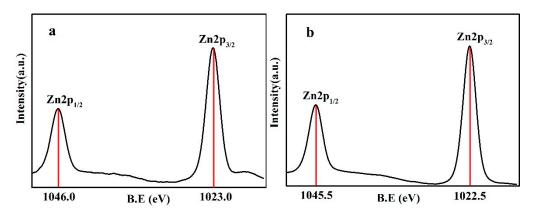


**Figure 6.** XPS of (**a**) ZnO–SiO$_2$-pH5.0; (**b**) ZnO–SiO$_2$-pH7.0.

**Table 2.** Element analysis based on XPS results

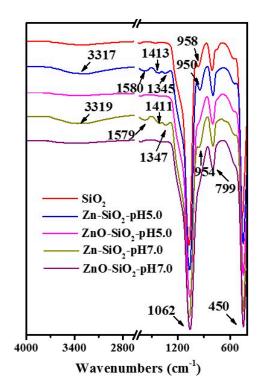| Samples | C1s (%) | Zn2p (%) | Si2p (%) | O1s (%) | O/Si |
|---|---|---|---|---|---|
| Amorphous SiO$_2$ | 2.74 | 0 | 31.27 | 65.84 | 2.11 |
| Zn–SiO$_2$-pH5.0 | 6.18 | 2.24 | 27.55 | 62.04 | 2.25 |
| ZnO–SiO$_2$-pH5.0 | 3.48 | 2.47 | 30.03 | 63.68 | 2.12 |
| Zn–SiO$_2$-pH7.0 | 6.90 | 6.24 | 24.38 | 60.84 | 2.50 |
| ZnO–SiO$_2$-pH7.0 | 5.96 | 10.55 | 25.18 | 58.39 | 2.31 |



**Figure 7.** FTIR spectra of amorphous SiO$_2$, Zn–SiO$_2$-pH5.0, ZnO–SiO$_2$-pH5.0, Zn–SiO$_2$-pH7.0, and ZnO–SiO$_2$-pH7.0.

Figure 8 shows a schematic diagram of the synthesis process of ZnO–SiO$_2$ by loading Zn$^{2+}$ on the amorphous SiO$_2$ carrier via the hydrothermal reaction and composite precursor calcination. Due to

the large number of Si–OH bonds on the surface of $SiO_2$ and the strong activity of Si–OH bonds, the interaction between Si–OH and Zn–OH is greater than the interaction in Zn–OH (multinuclear ions). Therefore, $Zn^{2+}$ is immobilized on the surface of $SiO_2$ and dispersed ZnO nanoparticles are formed after the calcination of precursors.
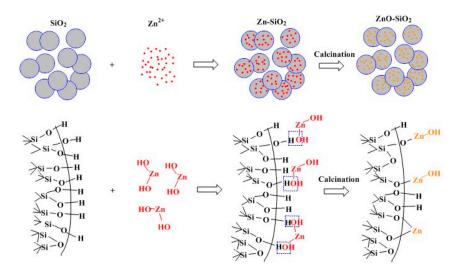


**Figure 8.** Synthesis of the $ZnO–nSiO_2$ Complex

### 3.2. Antibacterial Properties of $ZnO–SiO_2$

ZnO has antibacterial activity under light and dark conditions and is mostly applied under dark conditions. In order to investigate the antibacterial properties of $ZnO–SiO_2$ under dark conditions, $ZnO–SiO_2$-pH5.0, $ZnO–SiO_2$-pH7.0, and pure ZnO were respectively prepared. Figure 9 shows the bacterial growth profiles obtained by the plate test. Obvious colonies were formed in the blank control without the antimicrobial material (Figure 9a). When the concentration of $ZnO–SiO_2$-pH5.0 was 10 mg/mL, obvious colonies were observed on the culture plate; when the concentration of $ZnO–SiO_2$-pH5.0 was 20 mg/mL, the number of colonies decreased but colonies did not completely disappear; when the concentration of $ZnO–SiO_2$-pH5.0 was increased to 36 mg/mL, no colony was formed (Figure 9b). The concentrations of $ZnO–SiO_2$-pH7.0 and pure ZnO required for colony-free results were respectively 19 mg/mL and 20 mg/mL (Figure 9c,d). Based on the above results, the minimum inhibitory concentration (MIC) of each sample was determined and converted into the minimum inhibitory concentration of ZnO based on the content of ZnO in the composite (Table 3). The MIC values of $ZnO–SiO_2$-pH5.0 and $ZnO–SiO_2$-pH7.0 were respectively 1.60 and 2.14 mg/mL, which were equivalent to 10% of the MIC of pure ZnO (20 mg/mL), indicating that the antimicrobial ability of ZnO nanoparticles loaded on the $SiO_2$ surface was about 10 times that of pure ZnO. Obviously, the formation of dispersed nanoparticles (3–8 nm) loaded on amorphous $SiO_2$ greatly improved its antimicrobial performance.

**Table 3.** MIC of $ZnO–SiO_2$-pH5.0, $ZnO–SiO_2$-pH7.0, and pure ZnO.

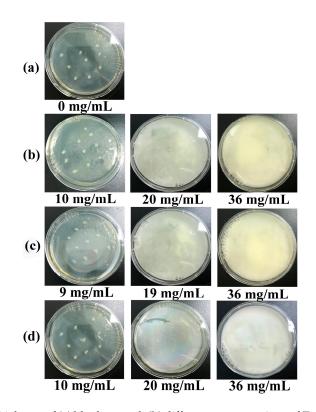| MIC (mg/mL) | $ZnO–SiO_2$-pH5.0 | $ZnO–SiO_2$-pH7.0 | ZnO |
|---|---|---|---|
| *E. coli* | 36 | 19 | 20 |
| *E. coli* (ZnO) | 1.60 | 2.14 | 20 |

**Figure 9.** Antimicrobial tests of (**a**) blank control, (**b**) different concentrations of ZnO–SiO$_2$-pH5.0 in agar medium, (**c**) different concentrations of ZnO–SiO$_2$-pH7.0 in agar medium, (**d**) different concentrations of pure ZnO in agar medium.

Figure 10 shows the antibacterial rate and colony growth conditions of *E. coli* on the plates added with different amounts of ZnO–SiO$_2$-pH7.0 coating. The antibacterial rate of the coating without ZnO–SiO$_2$-pH7.0 was 0 and a large number of colonies were formed on the plate, indicating that the coating showed no antibacterial property. When the addition of ZnO–SiO$_2$-pH7.0 in the coating was only 2%, the antibacterial rate was increased above 70%, showing a good antibacterial effect; when the dosage was gradually increased to 8%, the antibacterial rate of the coating to *E. coli* was 90.48%, which met the requirements of the antibacterial effect of antibacterial coating in Chinese national standard GBT21866-2008. The increasing antibacterial rate of the paint indicated less colonies and a better antibacterial effect.
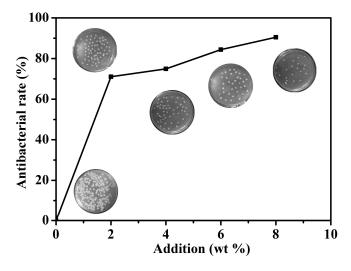


**Figure 10.** Effects of different additives on antibacterial rate (*E. coli*).

The antimicrobial properties of the ZnO nanoparticles supported uniformly and dispersedly on the surface of $SiO_2$ were greatly improved, due to the large specific surface area and surface activity of ZnO nanoparticles compared with the pure ZnO of large particles, and the contact and inhibition with microbes is stronger. This should be considered as one of the means to enhance the function of ZnO.

## 4. Conclusions

ZnO–$SiO_2$ composite was prepared by an environmentally friendly hydrothermal method and high-temperature calcination. In this composite, ZnO nanoparticles with a particle size of 3–8 nm were uniformly and dispersedly loaded on the surface of amorphous $SiO_2$. The size of the ZnO particles used in the industry is about 500 nm, and there is a certain degree of agglomeration among particles. According to the analysis of relevant tests, the strong interaction between the $SiO_2$ carrier surface and Zn–OH (precursors of ZnO) reduced the combination between Zn–OH, prevented its aggregation and formed monodispersed nanoparticles. Compared with pure ZnO, ZnO–$SiO_2$ showed much better antibacterial performance in the MIC test and the characterization test of paint properties.

In general, ZnO nanoparticles loaded uniformly and depressively on the surface of amorphous $SiO_2$ greatly enhanced its antibacterial function.

**Author Contributions:** Ying Chen and Hao Ding conceived and designed the experiments; Ying Chen performed the experiments; Ying Chen, Hao Ding and Sijia Sun anamyzed the date; Hao Ding contributed reagents/materials/analysis tools; Ying Chen wrote the paper.

**Conflicts of Interest:** The authors declare no competing financial interest.

## References

1. Ficociello, G.; Zanni, E.; Cialfi, S.; Aurizi, C.; Biolcati, G.; Palleschi, C.; Talora, C.; Uccelletti, D. Glutathione S-transferase θ-subunit as a phenotypic suppressor of *pmr1Δ* strain, the *Kluyveromyces lactis* model for Hailey-Hailey disease. *Biochim. Biophys. Acta* **2016**, *1863*, 2650–2657. [CrossRef] [PubMed]
2. Zanni, E.; Laudenzi, C.; Schifano, E.; Palleschi, C.; Perozzi, G.; Uccelletti, D.; Devirgiliis, C. Impact of a Complex Food Microbiota on Energy Metabolism in the Model Organism *Caenorhabditis elegans*. *BioMed Res. Int.* **2015**, *2015*, 621709. [CrossRef] [PubMed]
3. Uccelletti, D.; Zanni, E.; Guerisoli, M.; Palleschi, C. Caenorhabditis elegans: an emerging animal model for biomonitoring environmental toxicity. *J. Biotechnol.* **2010**, *150*, 257. [CrossRef]
4. Malachová, K.; Praus, P.; Rybková, Z.; Kozák, O. Antibacterial and antifungal activities of silver, copper and zinc montmorillonites. *Appl. Clay Sci.* **2011**, *53*, 642–645. [CrossRef]
5. Zanni, E.; Chandraiahgari, C.R.; Bellis, G.D.; Montereali, M.R.; Armiento, G.; Ballirano, P.; Polimeni, A.; Sarto, M.S.; Uccelletti, D. Zinc Oxide Nanorods-Decorated Graphene Nanoplatelets: A Promising Antimicrobial Agent against the Cariogenic Bacterium *Streptococcus mutans*. *Nanomaterials* **2016**, *6*, 179. [CrossRef] [PubMed]
6. Li, Y.; Zhang, W.; Niu, J.; Chen, Y. Mechanism of Photogenerated Reactive Oxygen Species and Correlation with the Antibacterial Properties of Engineered Metal-Oxide Nanoparticles. *ACS Nano* **2012**, *6*, 5164–5173. [CrossRef] [PubMed]
7. Cha, S.H.; Hong, J.; Mcguffie, M.; Yeom, B.; Vanepps, J.S.; Kotov, N.A. Shape-Dependent Biomimetic Inhibition of Enzyme by Nanoparticles and Their Antibacterial Activity. *ACS Nano* **2015**, *9*, 9097–9105. [CrossRef] [PubMed]
8. Vincenzini, P. *Ceramic Powders*; Elsevier Scientific Pub. Co: New York, NY, USA, 1983; Volume 16, pp. 843–849.
9. Wang, M.-H.; Ma, X.-Y.; Jiang, W.; Zhou, F. Synthesis of doped ZnO nanopowders in alcohol–water solvent for varistors applications. *Mater. Lett.* **2014**, *121*, 149–151. [CrossRef]
10. Chen, Y.; Kim, M.; Lian, G.; Johnson, M.B.; Peng, X. Side reactions in controlling the quality, yield, and stability of high quality colloidal nanocrystals. *J. Am. Chem. Soc.* **2005**, *127*, 13331–13337. [CrossRef] [PubMed]

11.   Pacholski, C.; Kornowski, A.; Weller, H. Self-Assembly of ZnO: From Nanodots to Nanorods. *Angew. Chem. Int. Ed.* **2002**, *41*, 1188–1191. [CrossRef]

12.   Choi, S.H.; Kim, E.G.; Park, J.; An, K.; Lee, N.; And, S.C.K.; Hyeon, T. Large-Scale Synthesis of Hexagonal Pyramid-Shaped ZnO Nanocrystals from Thermolysis of Zn-Oleate Complex. *J. Phys. Chem. B* **2005**, *109*, 14792–14794. [CrossRef] [PubMed]

13.   Pacholski, C.; Kornowski, A.; Weller, H. ZnO nanorods: Growth mechanism and anisotropic functionalization. In Proceedings of the SPIE 49th Annual Meeting on Optical Science and Technology, Denver, CO, USA, 2–6 August 2004.

14.   Ito, M.; Fukahori, S.; Fujiwara, T. Adsorptive removal and photocatalytic decomposition of sulfamethazine in secondary effluent using $TiO_2$-zeolite composites. *Environ. Sci. Pollut. Res. Int.* **2014**, *21*, 834–842. [CrossRef] [PubMed]

15.   Hassani, A.; Khataee, A.; Karaca, S.; Karaca, C.; Gholami, P. Sonocatalytic degradation of ciprofloxacin using synthesized $TiO_2$ nanoparticles on montmorillonite. *Ultrason. Sonochem.* **2017**, *35*, 251–262. [CrossRef] [PubMed]

16.   Xu, K.; Sun, Q.; Guo, Y.; Zhang, Y.; Dong, S. Preparation of super-hydrophobic white carbon black from nano-rice husk ash. *Res. Chem. Intermed.* **2013**, *40*, 1965–1973. [CrossRef]

17.   Chen, Y.; Peng, Z.; Kong, L.X.; Huang, M.F.; Li, P.W. Natural rubber nanocomposite reinforced with nano silica. *Polym. Eng. Sci.* **2008**, *48*, 1674–1677. [CrossRef]

18.   Khorsand Zak, A.; Majid, W.H.A.; Ebrahimizadeh Abrishami, M.; Yousefi, R.; Parvizi, R. Synthesis, magnetic properties and X-ray analysis of $Zn_{0.97}X_{0.03}O$ nanoparticles (X = Mn, Ni, and Co) using Scherrer and size-strain plot methods. *Solid State Sci.* **2012**, *14*, 488–494. [CrossRef]

19.   Jones, N.; Ray, B.; Ranjit, K.T.; Manna, A.C. Antibacterial activity of ZnO nanoparticle suspensions on a broad spectrum of microorganisms. *FEMS Microbiol. Lett.* **2008**, *279*, 71–76. [CrossRef] [PubMed]

20.   Tam, K.H.; Djurišić, A.B.; Chan, C.M.N.; Xi, Y.Y.; Tse, C.W.; Leung, Y.H.; Chan, W.K.; Leung, F.C.C.; Au, D.W.T. Antibacterial activity of ZnO nanorods prepared by a hydrothermal method. *Thin Solid Films* **2008**, *516*, 6167–6174. [CrossRef]

21.   Zhong, Z.; Zhe, X.; Sheng, T.; Yao, J.; Xing, W.; Yong, W. Unusual Air Filters with Ultrahigh Efficiency and Antibacterial Functionality Enabled by ZnO Nanorods. *ACS App. Mater. Interfaces* **2015**, *7*, 21538–21544. [CrossRef] [PubMed]

22.   Schwalbe, R.; Steele-Moore, L.; Goodwin, A.C. *Antimicrobial Susceptibility Testing Protocols*; CRC Press: Boca Raton, FL, USA, 2007.

23.   Test Method and Effect for Antibacterial Capability of Paints Film. Available online: http://c.gb688.cn/bzgk/gb/showGb?type=online&hcno=BD23209B12F6B07650FD542B0EB1456A (accessed on 1 October 2008).

24.   Zuo, Z.; Liao, R.; Zhao, X.; Song, X.; Qiao, Z.; Guo, C.; Zhuang, A.; Yuan, Y. Anti-frosting performance of superhydrophobic surface with ZnO nanorods. *Appl. Therm. Eng.* **2017**, *110*, 39–48. [CrossRef]

25.   Perillo, P.M.; Atia, M.N.; Rodríguez, D.F. Effect of the reaction conditions on the formation of the ZnO nanostructures. *Phys. E Low-Dimens. Syst. Nanostruct.* **2017**, *85*, 185–192. [CrossRef]

26.   Al-Gaashani, R.; Radiman, S.; Daud, A.R.; Tabet, N.; Al-Douri, Y. XPS and optical studies of different morphologies of ZnO nanostructures prepared by microwave methods. *Ceram. Int.* **2013**, *39*, 2283–2292. [CrossRef]

27.   Gallegos, M.V.; Peluso, M.A.; Thomas, H.; Damonte, L.C.; Sambeth, J.E. Structural and optical properties of ZnO and manganese-doped ZnO. *J. Alloys Compd.* **2016**, *689*, 416–424. [CrossRef]

28.   Gao, H.; Song, Z.; Yang, L.; Wu, H. Synthesis Method of White Carbon Black Utilizing Water-Quenching Blast Furnace Slag. *Energy Fuels* **2016**, *30*, 9645–9651. [CrossRef]

29.   Ghotbi, M.Y. Synthesis and characterization of nano-sized $\varepsilon$-$Zn(OH)_2$ and its decomposed product, nano-zinc oxide. *J. Alloys Compd.* **2010**, *491*, 420–422. [CrossRef]

30.   Hubert, C.; Naghavi, N.; Canava, B.; Etcheberry, A. Zinc Sulfide Based Chemically Deposited Buffer Layers for Electrodeposited CIS Solar Cells. In Proceedings of the Conference Record of the 2006 IEEE 4th World Conference on Photovoltaic Energy Conversion, Waikoloa, HI, USA, 7–12 May 2006.

31. Nie, H.; He, A.; Zheng, J.; Xu, S.; Li, J.; Han, C.C. Effects of Chain Conformation and Entanglement on the Electrospinning of Pure Alginate. *Biomacromolecules* **2008**, *9*, 1362–1365. [CrossRef] [PubMed]

32. Tai, Y.; Qian, J.; Zhang, Y.; Huang, J. Study of surface modification of nano-SiO$_2$ with macromolecular coupling agent (LMPB-g-MAH). *Chem. Eng. J.* **2008**, *141*, 354–361. [CrossRef]